Energy efficient monopod running with large payload based on open loop parallel elastic actuation

Fabian Guenther[1] and Fumiya Iida[2]

***Abstract*—Despite the intensive investigations in the past, energetic efficiency is still one of the most important unsolved challenges in legged robot locomotion. This paper presents an unconventional approach to the problem of energetically efficient legged locomotion by applying actuation for spring mass running. This approach makes use of mechanical springs incorporated in parallel with relatively low-torque actuation, which is capable of both accommodating large payload and locomotion with low power input by exploiting self-excited vibration. For a systematic analysis, this paper employs both simulation models and physical platforms. The experiments show that the proposed approach is scalable across different payload between 0 and 150kg, and able to achieve a total cost of transport (TCOT) of 0.10, which is significantly lower than the previous locomotion robots and most of the biological systems in the similar scale, when actuated with the near-to natural frequency with the maximum payload.**

I. INTRODUCTION

Legged locomotion is an important mode of mobility for robotic systems especially in highly constrained environment such as unstructured and uncertain rough terrains. While we witnessed the significant improvement in control of legged robots in the last decade, there has been only relatively slow progress in the investigation of energy efficiency, even though it is an equally important problem.

In general legged robots have been known to require orders of magnitude more energy for locomotion if compared to the biological systems in the similar sizes and weights. This line of investigations was pioneered by Gabrielli and von Karman in 1950s [1], where the definition of specific resistance (also known as cost of transport, COT) was introduced to compare energy efficiency among various biological and man-made systems. The work was extended by Tucker [2] and Kuo [3] by comparing energy efficiency with respect to body masses. These investigations showed that biological systems of similar weights exhibit the similar range of COT although most of legged robots require significantly more.

The majority of energy efficiency researches was reported in the context of bipedal robot walking [4], [5] (and running, [6]). Here the efficiency is measured with respect to the so-called total cost of transportation (TCOT), which refers to the total use of energy including both mechanical and electrical which is standardized by unit mass and unit travel distance. The current record of TCOT reported so far was achieved by the Cornell Biped ([4], TCOT $= 0.2$) and the Cornell Ranger ([5], TCOT $= 0.19$), both robots based on articulated rigid legs.

For running and hopping locomotion, Spring Loaded Inverted Pendulum (SLIP) has been investigated thoroughly in the past [7], [8]. This approach makes use of series elastic actuators [9], i.e. mechanical springs are installed between motors and leg structures, which play a role of shock absorbers as well as energetic buffers to recover some of the kinetic energy over multiple steps. The reported record of this approach (by [10], and [11]) was a mechanical COT of 0.22 and 0.2, respectively. Though not relying on mechanical springs, the MIT Cheetah robot reported an impressive achievement of TCOT 0.5 [12], even though the efficiency is still far from those of the biological systems. Parallel elasticity was investigated for spine [13], [14] and leg actuation [15] on several occasions. However, investigations on its influences to energetic efficiency of leg actuation have just yet started [16]. In general, there is still no commonly agreed principles about the use of mechanical dynamics for locomotion with various speed and body mass.

In this paper, we investigate an approach that make use of parallel elastic actuation for the purpose of energetic efficiency of hopping locomotion. Unlike the other models investigated in the past, this approach makes use of a mechanical spring incorporated in parallel with relatively low-torque actuator, which is used as the main drive of locomotion. The mechanical spring here can be used to support the variations of payload while it can trigger self-excited vibration for the purpose of locomotion. Through the analysis in simulation and physical robot platform, we will show that this approach enables hopping locomotion with significantly better energy efficiency beyond the existing robots and animals.

Please note that this paper is an extension of our previous work [17], [18]. We have both extended simulation and real-world experiments in order to thoroughly analyze the proposed approach. The rest of the paper is structured as follows: Section II describes the detailed design and physical modeling of the robot. Simulation setup and simulation experiments are presented in Section III. Section IV describes the design of the physical platform which is used in Section V to confirm the simulation results and measure the payload carrying performance, followed by discussion and conclusion.

II. DESIGN AND MODELING

This Section describes the physical model of Cargo used for simulations and introduces the strategies for payload attachment and actuation.

*This study was supported by the Swiss National Science Foundation Grant No. PP00P2123387/1 and the Swiss National Science Foundation through the National Centre of Competence in Research Robotics.

[1]F. Günther is with Institute of Robotics and Intelligent Systems, ETH Zurich, and with Bio-Inspired Robotics Laboratory, Department of Engineering, Cambridge University fabiangu@ethz.ch

[2] F. Iida is with Bio-Inspired Robotics Laboratory, Department of Engineering, Cambridge University fi224@cam.ac.uk

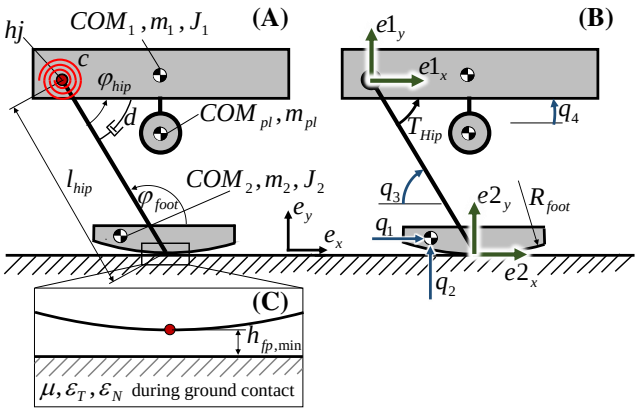

Fig. 1: Illustration of the physical model (A,B) and the ground contact setup (C, see Section III-A) of Cargo used for the simulations.

A. Physical model

In contrast to Cornell Ranger [5] and Cornell Biped [4], which are both walkers with rigid legs, Cargo is realized as a compliant monopod runner with a two-segmented leg and a curved foot, similar to [18]. The physical model of Cargo (Fig. 1) is planar and consists of two rigid bodies (lower and upper leg) with mass (m_1, m_2), center of mass $(\mathrm{COM}_1, \mathrm{COM}_2)$, and rotational inertia (J_1, J_2). Payload is modeled as a point mass $(m_{\mathrm{pl}}, \mathrm{COM}_{\mathrm{pl}})$ and rigidly attached to the upper leg. Upper and lower leg are connected with a rotational hip joint on which a linear torsional spring is attached. On the hip joint, a motor torque can be applied in parallel to the spring. The losses of the spring mechanism are modeled by a linear rotational damper in the joint. The lower body is equipped with a curved foot which establishes ground contact during stance phase.

The curved foot is designed as a circle with constant radius, and its purpose is to introduce self stabilizing dynamics to the system, in order to reduce sensing and control effort. Curved feet in general can improve both robustness and energy efficiency of walking [19], [4] and running [20], [21], [18], [22]. The same principle can be observed in nature as human feet roll over the ground during walking, similar to a wheel [23], [24].

Between ground and foot, dynamic friction with friction coefficient μ and impact with restitution factor $\epsilon_{\mathrm{N}}, \epsilon_{\mathrm{T}}$ occur during stance. The rest leg length of Cargo, defined as the distance between ground contact point and COM with the spring at rest length and the robot being balanced, is $L_{\mathrm{leg,rest}} = 0.36\,\mathrm{m}$. The weight distribution of the robot is designed in a way that, when standing on the ground in *initial posture* (Fig. 2), the upper body is roughly horizontal. Previous research [18] indicated that a more horizontal upper body angle is beneficial in terms of energy efficiency.

The payload of Cargo consists of weight plates up to $0.45\,\mathrm{m}$ diameter and is attached at a fixed point on the upper body and able to rotate freely around the z-axis. When standing in initial posture, this fixed point lies in line with the robot center of mass and the foot contact point. The robot is balanced without payload (Fig. 2 left), and the lower body angle with respect to the ground does not change significantly when adding payload (Fig. 2 right).

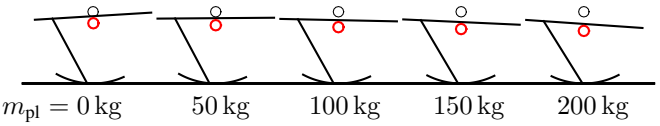

Fig. 2: Illustration of the initial robot posture depending on the payload without hip torque input. The red circle marks the center of mass of the robot, the black circle represents the center of the foot circle.

In order to reduce vertical impact losses, low mass of upper and lower body of Cargo is desirable. Since reduced stress on the structure is key towards the goal of low mass, long stance phases with low vertical accelerations and therefore low stress on the structure would be beneficial. This can be accomplished by choosing a low spring stiffness. On the other hand, a stiff spring would minimize the posture change during bouncing on the ground and therefore ease the analysis. As a compromise, we chose the spring stiffness in a way that the hip angle oscillation remains within $\pm 0.52\,\mathrm{rad}$ $(\pm 30°)$, which allows for hopping with $150\,\mathrm{kg}$ payload and $35\,\mathrm{N\,m}$ hip torque. With the max. hip angle oscillation set, the necessary ground clearance of the weight plates finally determines the size of the robot which results in the parameter set displayed in Tab. I.

For the simulation, upper body and payload mass are considered as one body. While payload and upper body mass can simply be summed up:

$$m_{1\mathrm{pl}} = m_1 + m_{\mathrm{pl}}, \tag{1}$$

the total center of mass of the upper body $\vec{r}_{\mathrm{COM1pl}}$ in the inertial frame is calculated as follows:

$$\vec{r}_{\mathrm{COM1pl}} = \frac{m_1 \cdot \vec{r}_{\mathrm{COM1}} + m_{\mathrm{pl}} \cdot \vec{r}_{\mathrm{COMpl}}}{m_1 + m_{\mathrm{pl}}}. \tag{2}$$

The total inertia of the upper body $J_{1\mathrm{pl}}$ follows in a similar way

$$J_{1\mathrm{pl}} = J_{1,\mathrm{hj}} + |\vec{r}_{\mathrm{hj}}^{\,\mathrm{COMpl}}|^2 \cdot m_{\mathrm{pl}} - m_{1\mathrm{pl}} \cdot |\vec{r}_{\mathrm{hj}}^{\,\mathrm{COM1pl}}|^2. \tag{3}$$

with $\vec{r}_{\mathrm{hj}}^{\,\mathrm{COMpl}}$ being the distance between hip joint and payload COM in the inertial frame and $\vec{r}_{\mathrm{hj}}^{\,\mathrm{COM1pl}}$ the distance between hip joint and the total COM of the upper body.

Ground friction coefficient, hip joint damping, and gearbox efficiency, were validated using the physical prototype presented in Section IV-A. A dynamic friction coefficient of 0.23 between foot disc and ground was measured for the plywood foot sliding on the MDF surface of the test track. Static fricton on the same track was about 1.5 times higher. We merged both static and dynamic friction coefficient into a simulation friction coefficient of 0.28. The average damping coefficient was determined to $1.3\,\mathrm{N\,m\,s\,rad^{-1}}$ by measuring the passive swing motion of the robot after the run. The gearbox efficiency of 0.95 was calculated out of typical values for optimized spur and chain gears.

TABLE I: Model parameters

A_{hip}	Hip torque amplitude	$[0..55]\,\text{N m}$
$L_{\text{leg,rest}}$	Rest leg length	$0.36\,\text{m}$
P_{idle}	Power consumption of the on board computer	$2\,\text{W}$
P_{comp}	Idle power consumption of the motor controller	$0.1\,\text{W}$
R_{foot}	Foot radius	$0.42\,\text{m}$
R_{motor}	Electric resistance of the motor	$0.3\,\Omega$
c	Hip spring stiffness	$2276\,\text{N m rad}^{-1}$
d	Hip damping coefficient	$1.3\,\text{N m s rad}^{-1}$
f_{hip}	Hip torque frequency	$[0..6]\,\text{Hz}$
i_{gear}	Gear reduction	148
k_{m}	Motor torque constant	$0.0302\,\text{N m A}^{-1}$
l_{hip}	Hip length	$0.441\,\text{m}$
m_1	Upper body mass	$19.287\,\text{kg}$
m_2	Lower body mass	$13.687\,\text{kg}$
m_{pl}	Payload mass	$[0\,\text{kg}..200]\,\text{kg}$
${}_{\text{e1}}\vec{r}_{\text{COM1}}$	COM Position upper leg	$[0.355; 0.002]\,\text{m}$
${}_{\text{e2}}\vec{r}_{\text{COM2}}$	COM Position lower leg	$[-0.171; 0.308]\,\text{m}$
$\vec{r}_{\text{COMpl}}$	Payload COM	$[0.229; -0.043]\,\text{m}$
$\epsilon_{\text{N}}, \epsilon_{\text{T}}$	Normal and tangential restitution factor	0
η_{gear}	Gear efficiency	0.95
η_{c}	Motor controller efficiency	0.9
μ_{gr}	Ground friction coefficient	0.28
φ_{foot}	Foot angle	$2.123\,\text{rad}$
$\varphi_{\text{hip,rest}}$	Hip angle with torque spring at rest	$1.763\,\text{rad}$
$J_{\text{1,hj}}$	Upper body inertia at hip joint	$2.890\,\text{kg m}^2$
$J_{\text{2,hj}}$	Lower body inertia at hip joint	$0.627\,\text{kg m}^2$
$J_{\text{mot,hj}}$	Motor inertia with respect to the hip joint	$0.396\,\text{kg m}^2$
State variables		
$q(t)$	Generalized position coordinates	m, rad
$u(t)$	Generalized speed coordinates	m s^{-1}, rad s^{-1}
Simulation variables		
dt_{sim}	Simulation timestep	$[0.025..0.5]\,\text{ms}$

TABLE II: Limitations of the physical prototype

n_{max}	Maximum motor speed	$1257\,\text{rad s}^{-1}$
$I_{\text{mot,max}}$	Maximum continuous motor current	$8.27\,\text{A}$
$\Delta\varphi_{\text{hip,max}}$	Maximum hip deflection	$\pm 0.52\,\text{rad}$

B. Equations of motion

Similar to [18], the state of the physical model (Fig. 1) is expressed using generalized coordinates:

$$\mathbf{q} = (q_1\ q_2\ q_3\ q_4)^T \tag{4}$$

During flight phase, the equations of motion can be displayed as

$$\mathbf{M}d\dot{\mathbf{q}}(\mathbf{q}, t) - \mathbf{h}(\mathbf{q}, \dot{\mathbf{q}}, t)dt = 0 \tag{5}$$

with mass matrix $\mathbf{M}$ and $\mathbf{h}$ summing up gyroscopic accelerations and smooth, generalized forces, including hip actuation. During stance, the equations of motion are extended by the measure of the contact forces $d\mathbf{R}$ as proposed in [25]:

$$\mathbf{M}\ddot{\mathbf{q}} - \mathbf{h}dt - d\mathbf{R} = 0. \tag{6}$$

By defining system state dependent force laws for $d\mathbf{R}$, it is possible to set up an optimization problem (linear complementary problem) for the contact forces. We assumed a Newtonian impact behavior

$$v_{\text{N}}^{+} = -\epsilon_{\text{N}} \cdot v_{\text{N}}^{-}, \quad v_{\text{T}}^{+} = -\epsilon_{\text{T}} \cdot v_{\text{T}}^{-} \tag{7}$$

with $v_{\text{N}}^{-}, v_{\text{T}}^{-}$ being the normal/tangential velocities of the colliding body just before impact and $v_{\text{N}}^{+}, v_{\text{T}}^{+}$ the normal/tangential velocities right after impact. $\epsilon_{\text{N}}, \epsilon_{\text{T}}$ are the normal and tangential impact factors, which we assumed to be zero in our model. This results in no energy to be recovered from the unsprung mass. Friction on the ground is modeled using a simplified Coulomb friction with identical static and dynamic friction coefficient $\mu_{\text{s}} = \mu_{\text{d}} = \mu_{\text{gr}}$:

$$F_T = -sign(\vec{v}_{\text{fp}}) \cdot \mu_{\text{gr}} \cdot F_{\text{N}}, \tag{8}$$

with F_{N} being the normal and F_{T} being the tangential component of the foot contact force. Once the solution for the linear complementary problem is found, we can re-enter the contact forces in Eq. (6) and integrate normally.

C. Actuation strategy

The hip joint of Cargo is actuated by using open loop clock torque control [26] in a parallel elastic configuration, in which a linear rotational spring is implemented in parallel with a linear damper and a back-drivable actuator. The actuator provides a sinusoidal hip torque on the joint

$$T_{\text{hip}}(t) = A_{\text{hip}} \cdot \sin(2 \cdot \pi \cdot f_{\text{hip}} \cdot t), \tag{9}$$

with amplitude A_{hip} and frequency f_{hip} as the two determining parameters. In Eq. (6) the hip actuation is integrated in the $\mathbf{h}$-vector as follows:

$$\mathbf{h} = (0\ 0\ T_{\text{hip}}\ T_{\text{hip}})^T + \mathbf{h}_{\text{other}}. \tag{10}$$

The motor torque which is necessary to create this hip torque is calculated by including gearbox efficiency η_{gear} as follows:

$$T_{\text{mot}} = \begin{cases} T_{\text{hip}}/\eta_{\text{gear}} & \text{if } T_{\text{hip}} \cdot \dot{\varphi}_{\text{hip}} > 0 \text{ (forward-drive)} \\ T_{\text{hip}} \cdot \eta_{\text{gear}} & \text{elsewhere (back-drive)} \end{cases}. \tag{11}$$

The mechanical motor power is calculated as:

$$P_{\text{mot}} = T_{\text{mot}} \cdot \dot{\varphi}_{\text{hip}} \tag{12}$$

The electric power input into the motor is calculated by using the electric DC motor model with torque constant k_{m}. By using motor current $I = \frac{T_{\text{mot}}}{k_{\text{m}}}$ and motor voltage $U = \dot{\varphi}_{\text{mot}} \cdot k_{\text{m}} + I \cdot R_{\text{mot}}$, electric motor power results in

$$P_{\text{el}} = P_{\text{mot}} + \left(\frac{T_{\text{mot}}}{k_m}\right)^2 \cdot R_{\text{mot}}. \tag{13}$$

The motor controller consumes an idle power $P_{\text{idle}} = 2\,\text{W}$ and has an efficiency of $\eta_{\text{c}} = 0.9$ for both forward- and back-drive. The on board computer consumes $P_{\text{comp}} = 0.1\,\text{W}$ which results in a total power consumption of:

$$P_{tot} = P_{\text{idle}} + P_{\text{comp}} + P_{\text{el}} \cdot \eta_{\text{c}}. \tag{14}$$

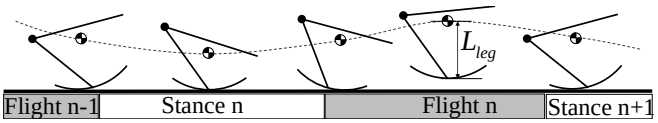

Fig. 3: Illustration of one step of successful running with the flight phase highlighted in grey for $m_{\text{pl}} = 100\,\text{kg}$. One step n starts at touchdown when the foot circle touches the ground and ends at the next touchdown $n+1$.

Positive P_{tot} thereby indicates that energy is consumed from the power supply, while negative P_{tot} indicates that energy is recovered into the power supply.

In the physical platform, motor speed, continuous motor current and hip spring deflection are limited according to Tab. II. For the implementation in the simulation, see Section III-D.

III. SIMULATION RESULTS

In this Section, we describe the simulated performance of Cargo for varying hip torque amplitude A_{hip}, hip torque frequency f_{hip}, and payload m_{pl}. After introducing the basic running pattern and stability behavior, we explore the robot's behavior at constant payload $m_{\text{pl}} = 100\,\text{kg}$ for different hip torque and frequency input and establish a filter process to separate periodic running solutions from other types of locomotion. Based on this data, we analyze the periodic running solutions in terms of efficiency and forward speed. And finally, we generalize these findings for variable payload.

A. Simulation setup

To solve the equations of motion (Eq. (6)) numerically, we implemented a time stepping algorithm based on the midpoint rule in MATLAB. Ground contact is modelled using one single contact point. This point lies on the foot disc vertically below the center of the disc. When the robot is moving, this contact point has not a fixed position on the foot disc but is recalculated for every simulation step (see Fig. 1C). As soon as the distance between contact point and ground becomes zero or negative, ground contact is established. With only one contact point, the number of cases for the linear complementary problem (LCP) is $2^{(3\cdot1)} = 8$, which allows for calculating all LCP cases until a solution is found. If no solution for the LCP was found for the default step size of $0.5\,\text{ms}$, the step size is bisected and the simulation step repeated, if necessary down to a step size of $0.025\,\text{ms}$. A simulation run always starts with the robot standing still in initial position position where body weight and spring torque are balanced and the COM of the system lies vertically over the contact point of the foot and the ground. Then the sinusoidal hip torque is applied for 50 cycles, starting from zero torque.

B. Running dynamics

Cargo is designed for forward running on level ground. One step of running (Fig. 3) starts at *touchdown* when the upper body bounces downward during *stance* phase and the torque spring in the hip joint gets compressed. After mid-stance, the upper body bounces back, gaining vertical speed

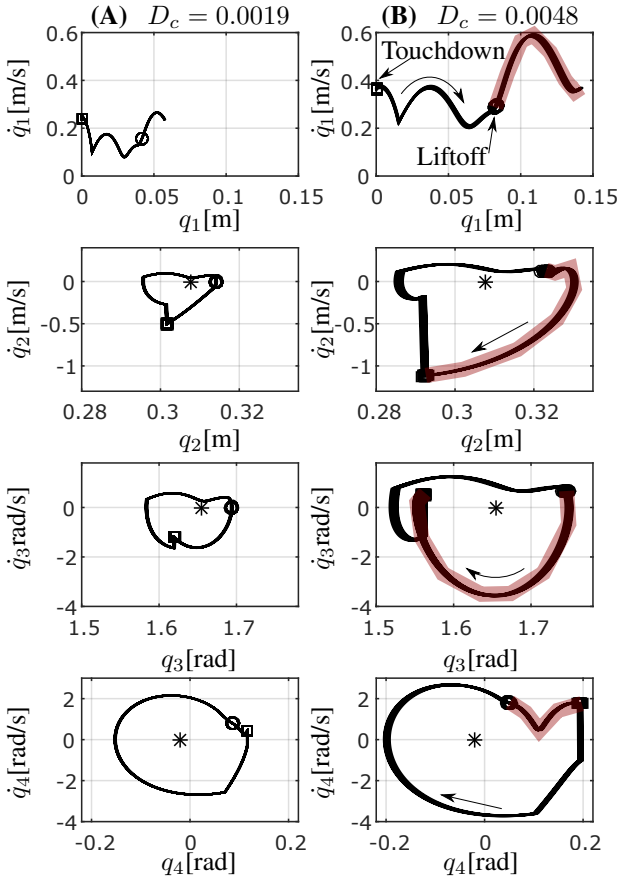

Fig. 4: Phase plots of the robot state variables and according cyclic deviation D_c during successful running. The stable fixed point is indicated with a *. **(A)** Last 25 steps of the run with lowest resulting cyclic deviation at $m_{\text{pl}} = 100\,\text{kg}, A_{\text{hip}} = 18\,\text{N m}, f_{\text{hip}} = 2.62\,\text{Hz}$. Touchdown of each step is indicated with a square, liftoff with a circle. The flight phase is highlighted in orange. **(B)** Last 25 steps of the run with highest cyclic deviation at $m_{\text{pl}} = 100\,\text{kg}, A_{\text{hip}} = 52\,\text{N m}, f_{\text{hip}} = 2.41\,\text{N m}$.

an counter-clockwise momentum for the following swing leg motion. During stance, rolling motion and sliding of the foot on the ground occur. At the end of the stance phase, the foot circle leaves the ground at *liftoff* and the upper body swings backwards during *flight* phase. When shutting down the motor input immediately during running, the robot takes one to three additional steps while continuously braking down to standstill. This running is entirely based on the robot's passive dynamic behavior and looks very similar to the actuated steady state running.

C. Running stability

With $100\,\text{kg}$ payload and no motor torque input, Cargo has a stable fixed point at $q^* = [0\ 0.308\ 1.655\ -0.022]^T$, which corresponds to its initial posture in Fig. 2. With an appropriate set of actuation parameters, Cargo exhibits stable running with small orbital deviations. As shown in phase plots (Fig. 4), the robot is capable of cyclic running behaviors, some of which

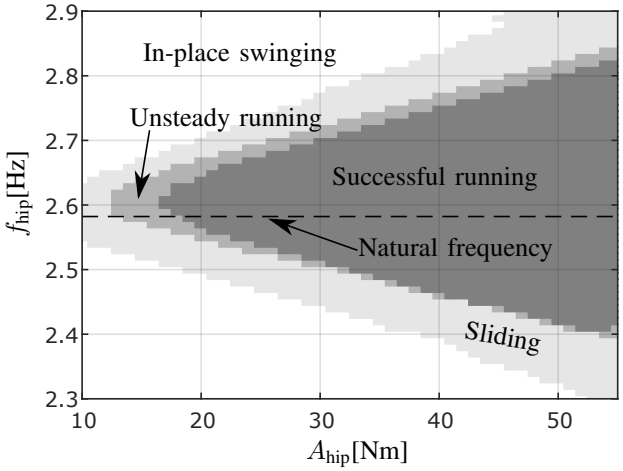

Fig. 5: Motion patterns for a given hip torque frequency f_{hip} and amplitude A_{hip} with $m_{\text{pl}} = 100\,\text{kg}$. All successful runs together shape the *successful running area*. Above $A_{\text{hip}} = 55\,\text{N m}$, the maximum motor current (see Tab. II) is exceeded and no successful hopping is possible. Outside of the successful running area, unsteady running, sliding or in-place swinging occurs.

are very stable (Fig. 4A), and the others with more deviations (Fig. 4B). On the phase plots, the impact at touchdown is the most prominent feature and can be located clearly for each state variable due to the sudden change in speed.

In order to quantify such deviations, here we introduce a metric called *cyclic deviation* defined as:

$$D_{\text{c}} = \sigma(q_{3,\text{touchdown}}) + \sigma(q_{4,\text{touchdown}}) \tag{15}$$

by summing up the averaged standard deviations of state variables q_3 and q_4 at touchdown. Visually, D_{c} is connected to the horizontal "thickness" of the line of the overlapped steps at touchdown. The thinner these line at touchdown, the lower D_{c} and the more uniform the run.

D. Conditions for successful running

Depending on the specific parameter choice of the motor input, Cargo performs forward running as well as in-place swinging and sliding locomotion[1]. A run starts with the sinusoidal hip torque (Eq. 10) being applied to the robot standing still in initial posture. This torque is then applied for 50 cycles before shutting down the power. When applying the hip torque, the robot first builds up the oscillation of the upper body, then accelerates and finally reaches steady state forward running for certain motor input. To separate periodic running solutions from all other types of locomotion, we use a filter process based on the 50 cycles of the motor torque during a simulation run:

1) The average horizontal speed of the robot COM needs to be positive for each of the last 25 motor torque cycles. Patterns without forward locomotion are called in-place swinging.
2) The robot must be in flight phase during at least one simulation time step during each of the last 25 motor torque cycles. The maximum hopping height needs to be at least $0.002\,\text{m}$ for each step. Patterns with forward speed but without any flight phases are called sliding. Patterns with forward speed but without enough or high enough flight phases are called unsteady running.
3) Motor and spring limitations (Tab. II) need to be fulfilled during all 50 motor torque cycles.
4) Within the last 25 motor torque cycles, the average forward speed of the fastest cycle must not be more than 1.2 times larger than the average forward speed of the slowest cycle. Any running pattern with larger forward speed deviation is called unsteady running.

We call every locomotion pattern which fulfills these conditions *successful running* and the associated simulation run and parameter set *successful run*.

To explore the robot's behavior for different hip torque parameters, we conducted simulation runs for each possible combination of hip torque amplitude A_{hip} and frequency f_{hip} with a resolution of $1\,\text{N m}$ and $0.1\,\text{Hz}$, respectively When displaying the successful runs in the motor torque amplitude-frequency plane (Fig. 5) a conical shape with the tip towards lower amplitude can be observed, which we call *successful running area*. The frequency at the tip is very close to the natural frequency of the robot, which occurs when the robot stands on the ground and swings passively. While successful running with minimum forward speed and foot clearance is only possible near this natural frequency, with increasing motor torque amplitude, the swinging amplitude around the hip increases too and enables higher energy input. With the actuator energy becoming larger with respect to the spring energy of the system, higher motor torque amplitudes allow for larger deviations from the natural frequency, and therefore a larger usable frequency range.

All successful runs we conducted so far show stable forward running (see Section III-C) and follow the pattern described in Section III-B. Fig. 4 thereby shows the lowest and highest cyclic deviation of all successful runs performed at $m_{\text{pl}} = 100\,\text{kg}$.

E. Energetic characteristics

The total cost of transport

$$\text{TCOT} = \frac{1}{n}\sum_{i=1}^{n}\frac{1}{m\cdot g}\cdot\frac{\int_i^{i+1} P_{\text{tot}}\cdot dt}{\int_i^{i+1} v_{\text{COMx}}\cdot dt} \tag{16}$$

describes the power spent per speed per body weight during n steps. For Cargo with $100\,\text{kg}$ payload, it distributes smoothly within the successful running area (Fig. 6A) with low values at the upper and lower border of the successful running area and a minimum of 0.1499 at minimum amplitude. Up to $A_{\text{hip}} = 46\,\text{N m}$, the upper border TCOT is slightly lower compared to the lower border TCOT, while this ratio reverses above $A_{\text{hip}} = 46\,\text{N m}$. Plotted separately (Fig. 6B), the best

[1]This paper has supplementary downloadable material available at http://ieeexplore.ieee.org, provided by the authors. This includes several MP4 format movie clips, showing animation of in-place swinging, sliding, unsteady forward running, and successful forward running.

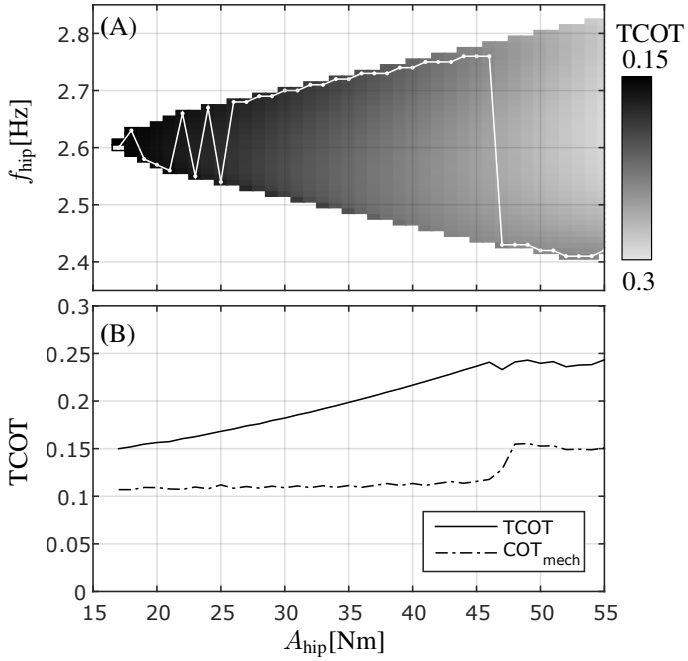

Fig. 6: **(A)** TCOT for a given hip torque frequency f_{hip} and amplitude A_{hip} at $m_{\text{pl}} = 100\,\text{kg}$, indicated using gray scale. The white line indicates minimum TCOT for each hip torque amplitude A_{hip}. **(B)** Minimum TCOT for each hip torque amplitude and corresponding COT_{mech}.

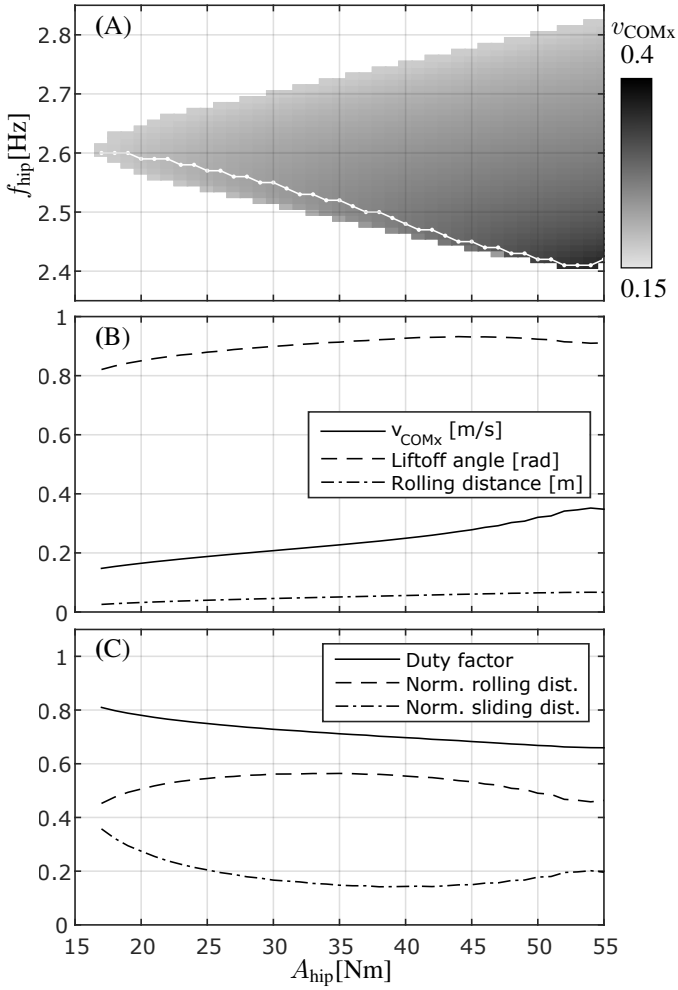

Fig. 7: **(A)** Simulated forward speed v_{COMx} at $m_{\text{pl}} = 100\,\text{kg}$ for a given hip torque frequency f_{hip} and amplitude A_{hip}, represented using grayscale. The white line marks the maximum v_{COMx} per amplitude. **(B)** Maximum v_{COMx} and corresponding liftoff angle per amplitude. **(C)** Duty factor, rolling distance and sliding distance, normalized with the step length.

TCOT per Amplitude increases with increasing amplitude up to $A_{\text{hip}} = 46\,\text{N m}$ and then remains nearly constant up to maximum amplitude.

The concept of COT can be applied to parts of the system too to display the energy consumption of subsystems in a dimensionless way. While the TCOT is based on the electrical energy input in the motor controller and on-board computer, the COT_{mech} for example is based on the mechanical energy output at the hip and therefore represents the efficiency of the robot mechanics neglecting the drivetrain. When plotting the minimum COT_{mech} against amplitude (Fig. 6B), it first remains nearly constant with a minimum value of 0.1069 along the upper border. Around $A_{\text{hip}} = 46\,\text{N m}$, it increases to its higher value along the lower border.

When hopping at minimum TCOT, the spring is doing the whole energy conversion during bouncing with a max spring torque of $629\,\text{N m}$ and a max. energy stored in the spring of $87\,\text{J}$. The motor is doing $98\,\%$ positive work with a total energy input of $8\,\text{J}$ at the hip.

F. Forward speed effects

The forward speed v_{COMx} is defined as the x-component of the COM speed vector. For Cargo with $100\,\text{kg}$ payload, the forward speed distributes smoothly in the successful running area (Fig. 7A) and increases with increasing amplitude and decreasing frequency. The hip torque amplitude can be used (in combination with appropriately tuned frequency) to directly influence the forward speed (Fig. 7B). The highest forward speed of $0.3519\,\text{m s}^{-1}$ is placed at the right lower border of the successful running area. The minimum possible forward speed of $0.1476\,\text{m s}^{-1}$ can be found at the left tip of the successful running area. Above $A_{\text{hip}} = 46\,\text{N m}$, the locations of the maximum forward speed per amplitude and the minimum TCOT per amplitude (see Fig. 6A) within the successful running area are similar.

The liftoff angle is defined as the angle of the robot COM speed vector at liftoff with respect to the horizontal plane. Cargo has a liftoff angle around $0.9\,\text{rad}$ $(52°)$ with slightly lower values towards lower amplitude.

The distance the foot contact point travels during stance is at the same time the length of the foot part which has actually ground contact. With values below $0.078\,\text{m}$ ($22\,\%$ of the leg length), the normalized effective foot length of Cargo is comparable to humans.

The duty factor or Cargo, which represents the ratio of stance time to total step time, decreases with increasing forward speed, i.e. the flight phases become longer compared to the stance phases (Fig. 7B). With a duty factor between 0.66 and 0.81, Cargo spends more time during stance compared to

other runners. The ARL Monopod II for example has values between 0.5 and 0.6 (Fig. 10 in [10]) and values for sprinters (both legs added up) lie between 0.4 and 0.72 (Fig. 3 in [27]).

During stance, rolling and sliding of the foot occur simultaneously. The normalized rolling distance indicates the ratio of the length which is traveled by the robot COM in x-direction while rolling, normalized by the step length. The sliding distance is defined accordingly. For very low amplitudes, the foot nearly slides as much as it rolls, while towards larger amplitudes rolling becomes dominant. To clarify the underlying reasons for this behavior, future investigations are necessary.

The maximum rolling distance of $0.0668\,\mathrm{m}$ corresponds to a lower leg angular change of $q_{3,\mathrm{liftoff}} - q_{3,\mathrm{touchdown}} = 0.185\,\mathrm{rad}$. If we now imagine Cargo with a point foot instead of the foot disc while keeping the leg length constant at $L = L_{\mathrm{leg,rest}}$, the same angular change would lead to a distance traveled by the COM of $0.0665\,\mathrm{m}$, nearly equal to the distance with the curved foot. Therefore, when compared to a point foot, the gain in traveled distance of the foot disc is negligible.

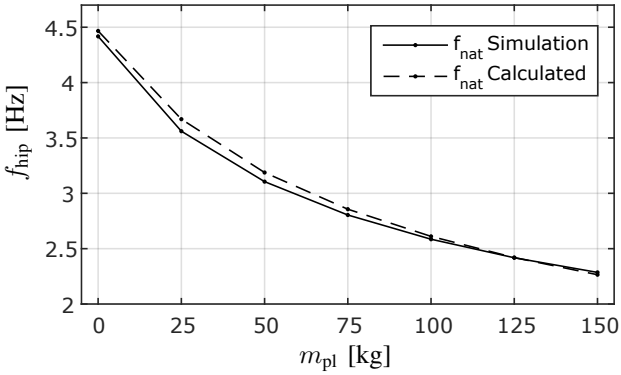

Fig. 8: First natural frequency f_{nat} of the simulation model of Cargo depending on the payload. Values out of simulation experiments and calculated using Eq. 17.

G. Influence of payload

Cargo is able to run successfully with additional payload between $0\,\mathrm{kg}$ and $150\,\mathrm{kg}$. Basic running dynamics (see Section III-B) thereby remain the same for all payloads. In this Section, we analyze the influence of additional payload to efficiency, speed and uniformity of the running locomotion of cargo.

As mentioned earlier, the natural frequency defines the frequency where locomotion with minimum TCOT occurs. This natural frequency can be determined by running a simulation without hip torque input, starting from standstill with the COM of the system vertically over the contact point of the foot and the ground. By setting the hip angle to $\varphi_{\mathrm{hip,rest}}$, the upper body swings passively and the hip angle oscillation corresponds to the natural frequency of the robot.

Since this natural frequency strongly depends on the upper body mass and therefore on the payload, the first step towards variable payload is to develop an estimation of this natural frequency. To do so, we neglect the lower body and assume the upper body to be fixed on a wall at the hip joint. The spring, initially acting between upper and lower body, is acting now between the wall and the upper body. In this configuration, the upper body forms a rotational spring mass system with stiffness c and inertia J_{1pl} from Eq. (3). The resulting natural frequency can be calculated as:

$$f_{\mathrm{nat}} = \frac{1}{2\pi}\sqrt{\frac{c}{J_{\mathrm{1pl}}}}. \tag{17}$$

The natural frequency per payload predicted by this simplified simulation model is similar to the natural frequency predicted by the complete simulation model (Fig. 8), with some deviations at low payloads.

With the calculated natural frequency, the hip torque input parameter search space for each payload is determined as follows:

$$A_{\mathrm{hip}} = [0, 1, .., 55]\,\mathrm{N\,m} \tag{18}$$

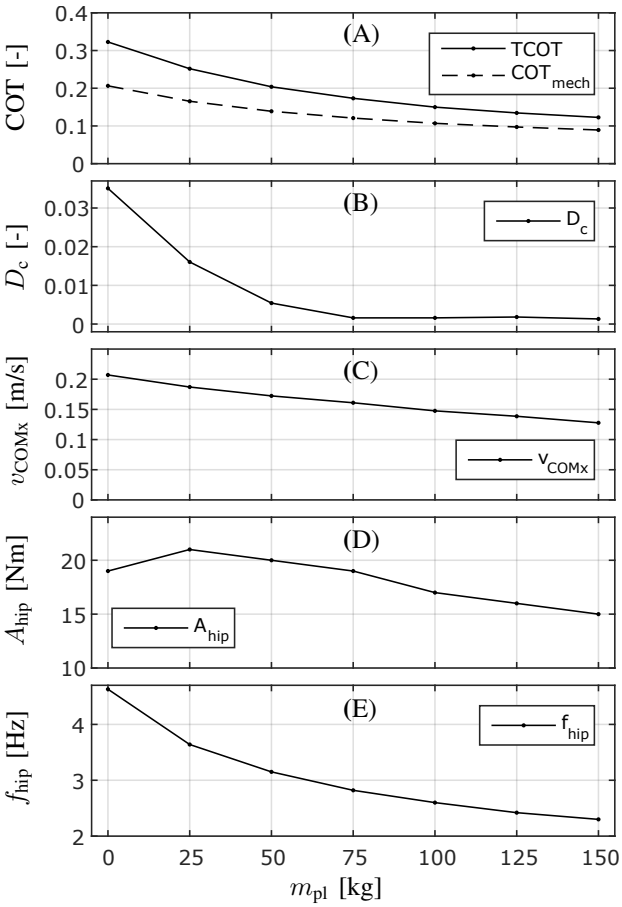

Fig. 9: Simulated performance of Cargo for payloads between 0 and $150\,\mathrm{kg}$. **(A)** Minimum total cost of transport $\mathrm{TCOT}_{\mathrm{min}}$ per payload. **(B)** Cyclic deviation D_{c} @ $\mathrm{TCOT}_{\mathrm{min}}$. **(C)** Forward speed v_{COMx} @ $\mathrm{TCOT}_{\mathrm{min}}$. **(D,E)** Amplitude and Frequency @ $\mathrm{TCOT}_{\mathrm{min}}$.

and

$$f_{\text{hip}}(m_{\text{pl}}) = f_{\text{nat}}(m_{\text{pl}}) \pm 1\,\text{Hz}. \quad (19)$$

To explore the influence of payload on Cargo, we conducted simulations for 9 different payloads between 0 and 200 kg. For each payload, simulation and analysis was performed in the same way as described for 100 kg before, within the hip torque parameter space defined by (18) and (19). As a result, Cargo is able to perform successful running with payloads between 0 and 150 kg. At $m_{\text{pl}} = 175\,\text{kg}$ the forward speed becomes unsteady and therefore no successful running is possible. For each payload $m_{\text{pl}} \in [0..150]\text{kg}$, the successful running area shows a similar shape as for $m_{\text{pl}} = 100\,\text{kg}$ (see Fig. 6) with smooth distribution and minimum TCOT at the left tip of the area and highest v_{COMx} in the right bottom area. Lower payloads allow larger deviations from the natural frequency for a certain amplitude, therefore the "opening angle" of the successful running area cone becomes larger for lower payloads.

Fig. 9 summarizes the TCOT_{min} for each payload and its corresponding parameters. The TCOT_{min} (Fig. 9A) decreases with increasing m_{pl} down to its best value of 0.1227 at $m_{\text{pl}} = 150\,\text{kg}$. The COT_{mech} decreases with payload as well and the efficiency of the drivetrain (motor, motor controller, gearbox), which can be estimated using $\text{COT}_{\text{mech}}/\text{TCOT}$, increases from 0.64 at 0 kg payload to 0.70 at 150 kg.

The corresponding cyclic deviation D_{c} (Fig. 9B) is low with the exception of 0 and 25 kg payload. At these low payloads, a slow overlaying forward/backward oscillation of the whole robot can be observed which causes the increased D_{c}. A similar behavior observed at the physical prototype can be seen in Fig. 13A.

The forward speed v_{COMx} at minimum TCOT for each payload (Fig. 9C) is at the same time the minimum possible forward speed for each payload. This speed decreases with increasing payload down to its minimum value of $0.1277\,\text{m}\,\text{s}^{-1}$ at $m_{\text{pl}} = 150\,\text{kg}$. The hip torque amplitude (Fig. 9D) behaves similar to the forward speed, except for a short increase between 0 and 50 kg payload.

As mentioned earlier, running at minimum TCOT means running near natural frequency. This holds true for all payloads with the frequency at minimum TCOT (Fig. 9E) being slightly above the natural frequency at that payload.

IV. PHYSICAL PLATFORM AND DATA ACQUISITION

We designed a physical platform to verify the simulation results. All parameters are similar similar to the ones of the simulation model (see Tab. I).

A. Experimental platform

The physical platform Cargo (Fig. 10) consists of an upper and lower body which are built using a modular system based on 50 mm aluminum tubes and custom aluminum clamping braces for joints, payload, spring attachment and tube connectors. This enables quick adaptation to new geometries without the need for manufacturing new parts. In addition it guarantees for high stiffness and enables the upper and lower body to be very close to rigid bodies. To avoid frictional losses which occur in a torsional spring setup, we realized the spring on the hip joint by using two helical tension spring pairs instead of a torsional spring (Fig. 11A). Within the work range, this setup approximates the torque spring setup with errors less than 2 % (Fig. 11B). Upper and lower spring were realized as spring pairs and all shafts are supported with ball bearings to further minimize losses.

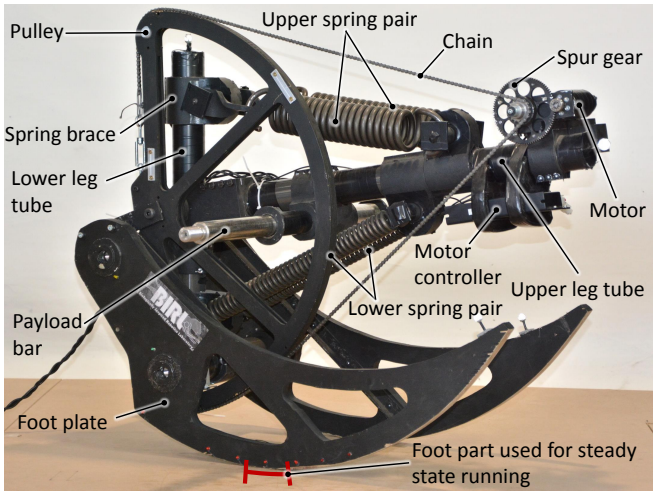

Fig. 10: Picture of the physical prototype of Cargo used for the experiments. All parameters are similar to the model used for the simulations.

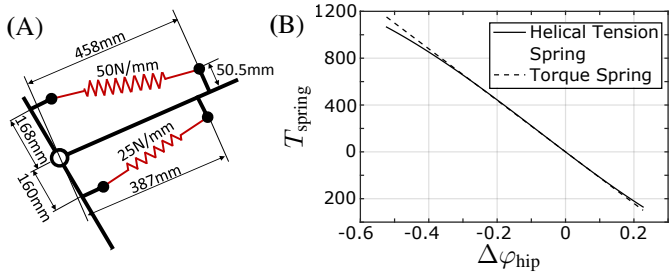

Fig. 11: **(A)** Helical tension spring mechanism at the hip of the physical prototype of Cargo. **(B)** Calculated spring curves for the torsional spring mechanism used for simulations and the helical tension spring mechanism used in the physical prototype.

The two foot plates are designed as circle segments made from 21 mm plywood with a collateral distance of 0.25 m. For convenience and safety, the foot plates are significantly enlarged. During steady state running, only 0.08 m of the sole of the foot has ground contact (see Fig. 10). For the payload, we chose commercial weight discs because of their good availability and easy handling. The whole robot was dimensioned to withstand the full tension of the upper springs (7522 N) with a safety margin > 2.

The two-stage gears of the motor consist of a chain drive (1st stage) and a spur gear (2nd stage) with a total gear reduction of 148. The large wooden chain pulley is rigidly

connected to the lower leg to allow the motor to drive the hip joint directly with the spring mechanism being in parallel. In the physical platform, the motor torque T_{mot} is sinusoidal, in contrast to the simulation, where the hip torque T_{hip} is sinusoidal. Due to the relation shown in Eq. (11), a sinusoidal motor torque results in a non-sinusoidal hip torque, depending on whether energy is flowing from the motor to the hip (forward-drive) or the other way around (back-drive). But since back-drive in Cargo occurs usually during less than $10\,\%$ of the stance time, the hip torque can be approximated using

$$T^*_{\text{hip}} \approx T_{\text{mot}} \cdot \eta_{\text{gear}}, \quad A^*_{\text{hip}} \approx A_{\text{mot}} \cdot \eta_{\text{gear}}. \tag{20}$$

B. Data acquisition

The motor of Cargo is torque controlled using the internal current controller provided by the EPOS motor controller. This allows to follow the target current up to 6Hz with differences lower than $5\,\%$. Voltage and current into the EPOS were sampled at $40\,\text{kHz}$ to provide information about the electric input power. The sinusoidal input signal for the motor controller was created using two different approaches. For wireless runs on the one hand, we used an on-board computer (Arduino Yun) with a power consumption of $0.1\,\text{W}$. For convenience and measurement purposes on the other hand, we conducted wired runs with the input signal created by a PC using MATLAB. For the calculation of the total input power, the power consumption of the on-board computer was added for both wired and wireless runs.

We used an OptiTrack motion capturing system to capture upper and lower body trajectories of the robot at 125 frames per second. The motion capture data was then used to calculate the generalized coordinates $q, \dot{q}$ and the forward speed v_{COMx}. For the position data q, the motion capturing data was used directly without filtering. For the velocity data $\dot{q}$, we used a mean average filter over five frames.

The motion capturing system is able to detect hopping heights down to $3\,\text{mm}$. To detect smaller hops, we used acoustic feedback since even small hopping heights down to $1\,\text{mm}$ lead to an acoustic impact.

All analysis of the physical data is based on the motor controller input, the generalized coordinates and the acoustic impact and was performed in the same way as described in Section III.

V. EXPERIMENTAL RESULTS

We conducted physical runs with Cargo similar to the simulation runs[2]. After starting from standstill by applying the sinusoidal motor torque input, the robot accelerates and stabilizes forward speed after 5 to 7 steps. Due to limitations of the test track, one run consists of 30 motor torque cycles and the last 15 cycles were used for analysis. After extracting the generalized coordinates $q, \dot{q}$ (see Eq. (4)) out of the motion capturing data, we synchronized them with the measured motor controller input power and determined the total cost of transport TCOT (16) and the forward speed v_{COMx} in the same way as we did for the simulation data. In addition, the definitions for the successful run (Section III-D) apply to the physical platform in the same way as for the simulation model. We conducted 3 to 5 runs per parameter set to determine mean values and standard deviation.

[2]This paper has supplementary downloadable material available at http://ieeexplore.ieee.org, provided by the authors. This includes two MP4 format movie clips, one showing run with $150\,\text{kg}$ payload from Fig. 16, and another showing the ground clearance in a closeup of the same run.

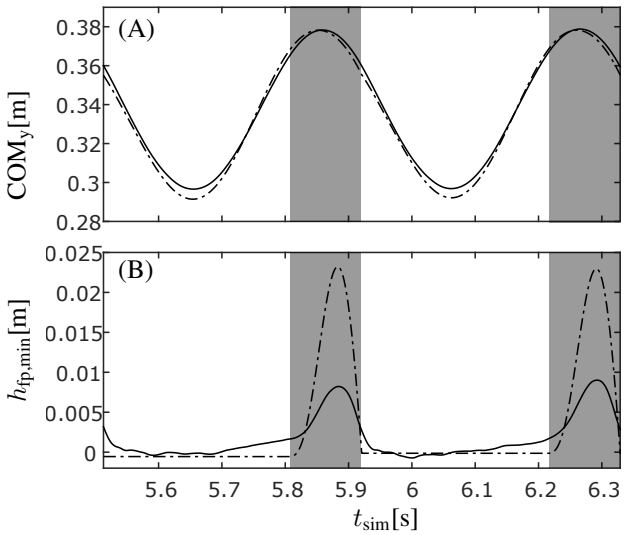

Fig. 12: Physical (solid) and simulated (dashed) trajectories of the robot COM (A) and the distance between foot and ground (B) for $m_{\text{pl}} = 100\,\text{kg}$, $A^*_{\text{hip}} = 44\,\text{N m}$, $f_{\text{hip}} = 2.45\,\text{Hz}$ for two steps.

A. Trajectories and running stability

During successful runs, the physical platform as well as the simulation model show a bouncing motion of the COM, which is typical for spring-mass systems (Fig. 12A). In addition, a flight phase can be observed in both cases (Fig. 12B). While the bouncing of the COM is similar for physical and simulation experiment, the simulation shows larger swinging around the hip during flight, which leads to larger ground clearance compared to the physical data.

When plotting phase plots of the experimental data (Fig. 13), the overall shape and localization within the parameter plane is similar to simulation data with identical parameters. Due to varying ground friction, the cyclic deviation D_{c} in the experiment is higher than in simulation. The physical upper body behavior (q_4) is well represented by the simulation, while (q_1) indicates that the touchdown occurs "later" in simulation, i.e. when q_1 is decreasing again. Larger differences occur in the flight phase swinging (q_3) and impact behavior (q_2) of the lower leg. In contrast to the simulation, the physical drivetrain has some elasticity, a non-ideal current controller and complex losses at low amplitudes, and we assume that this may cause the differences between simulation and experimental q_2 and q_3. Finally, the plot of q_2 to q_4 shows three similar patterns which are slightly shifted against each other along the x-axis. This represents a forward-backward rocking motion of the whole robot, affecting both upper and lower body.

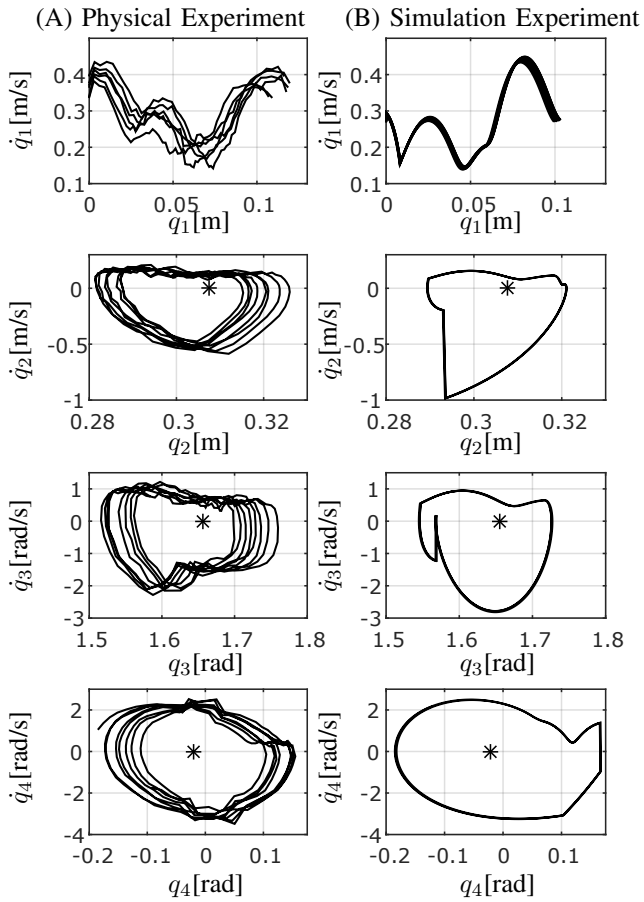

Fig. 13: Phase plot of the robot state variables $q, \dot{q}$ for $m_{\text{pl}} = 100\,\text{kg}$, $A^*_{\text{hip}} = 44\,\text{N m}$, $f_{\text{hip}} = 2.45\,\text{Hz}$. The stable fixed point is indicated with a *. (A) Physical values for 15 steps with $D_{\text{c}} = 0.0522$. (B) Simulation values for 25 steps with $D_{\text{c}} = 0.0033$.

During all physical experiments, the robot kept track very well, with a deviation to the left/right below $5\,\text{cm}$ over a $5\,\text{m}$ running distance.

B. Natural frequency

To validate the simulation model, we examined the natural frequency f_{nat} of the physical platform for different payloads and compared it with the simulation values. The natural frequency is thereby the oscillation of the upper body when standing on the ground. This frequency was measured by swinging up the robot by hand and then let the oscillation die out. The natural frequency of the physical platform thereby shows good match with the simulation data (Fig. 14).

C. Energetic characteristics and forward speed effects

In contrast to the simulation, we did not measure through the whole motor input space during the physical experiments. Instead, assuming that the shapes of simulated and physical successful running area are similar, we explored only the lower border of the area where the higher forward speeds are located. For the energetic characteristics and the forward velocity effects, we conducted measurements for five different

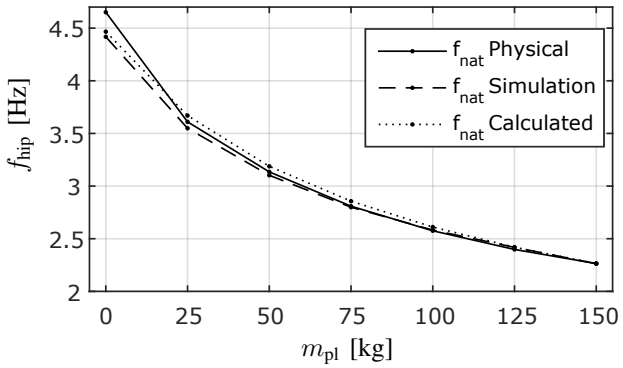

Fig. 14: First natural frequency f_{nat} of Cargo depending on the payload for physical and simulation experiment and calculated with Eq. 17.

amplitudes. For each amplitude, we executed various runs through the frequency-range around the lower border of the result plane. Based on this data, we reconstructed the lower border of the successful running area and extracted the minimum TCOT and the according v_{COMx} from this data.

One basic finding of the simulations was the fact that the minimum TCOT occurs at minimum amplitude and close to natural frequency. This could be confirmed with the experiments (Fig. 15A) with $100\,\text{kg}$ payload. In addition, the physical TCOT shows the expected increase towards larger hip torque amplitudes and physical and simulation TCOT match well at higher amplitudes. At lower amplitudes, however, the simulation overestimates the TCOT. Another finding from the simulations was that the hip torque amplitude can be used to control the forward speed. The physical platform shows the same behavior (Fig. 15B) as forward speed increases with enlarging amplitude. The physical experiment shows higher forward speed per amplitude and the speed difference to the simulation is nearly independent from the amplitude. To clarify the underlying reasons for this behavior, future investigations are necessary.

D. Influence of payload

In simulation, for each payload Cargo shows its best performance near natural frequency and minimum hip torque amplitude (see Section III-G). To find this point in the physical experiment, we slightly varied the hip torque frequency around the previously measured physical natural frequency and executed various runs with increasing amplitude, starting from $A^*_{\text{hip}} = 10\,\text{N m}$. For the analysis, we then considered the run with the lowest hip torque amplitude that has a clearly detectable flight phase for each step. To cover the whole payload range, we repeated this procedure for $m_{\text{pl}} = [0, 25, 50, 75, 100\,\text{kg}, 125, 150]\,\text{kg}$.

The results of the physical experiments for the best performance at different payloads as well as simulation results with identical motor input are shown in Fig. 16. Over the whole payload range except for 0, the physical prototype undercut the simulated TCOT by about 0.03. At $m_{\text{pl}} = 150\,\text{kg}$, a physical TCOT of 0.0994 was reached. The physical cyclic deviation shows the same decrease with increasing payload

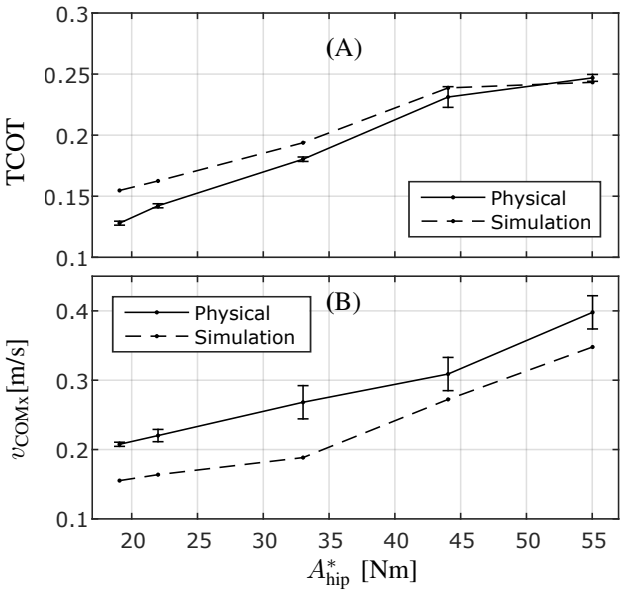

Fig. 15: **(A)** Physical and simulated TCOT_{min} of Cargo for hip torque amplitudes between $19\,\text{N}\,\text{m}$ and $55\,\text{N}\,\text{m}$ at $m_{\text{pl}} = 100\,\text{kg}$ and $f_{\text{hip}} = [2.58\ 2.56\ 2.50\ 2.45\ 2.42]\text{Hz}$. **(B)** Corresponding physical and simulated v_{COMx} for TCOT_{min}.

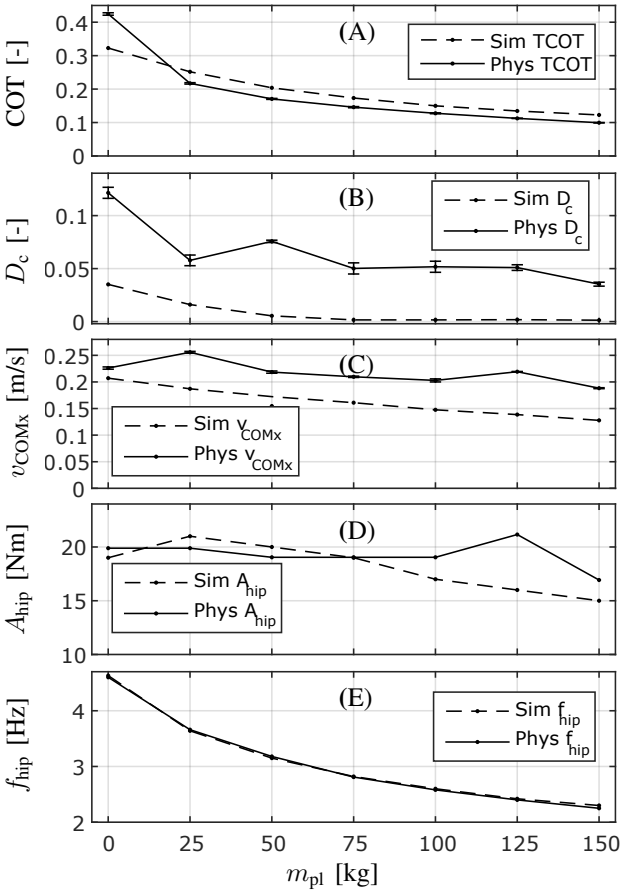

Fig. 16: Real world performance of Cargo at different payloads between 0 and $150\,\text{kg}$. **(A)** Minimum total cost of transport TCOT_{min} per payload. The lowest $\text{TCOT}_{\text{min}} = 0.0994$ is reached at $m_{\text{pl}} = 150\,\text{kg}$. **(B)** Cyclic deviation D_{c} @ TCOT_{min}. **(C)** Forward speed @ TCOT_{min}. **(D,E)** Amplitude and Frequency @ TCOT_{min}.

as in simulation, although is generally higher. The reason for this is probably the ground friction which slightly varies with each step in the physical experiment. The forward speed in simulation is in average $0.07\,\text{m}\,\text{s}^{-1}$ lower in simulation when compared to the physical experiment. As a result, the physical platform of Cargo realizes its TCOT per payload at higher input power, compared to simulation. As already indicated for $100\,\text{kg}$ payload in Fig. 15, the lower forward speed seems to be a universal difference between simulation and physical experiment, and future investigations are necessary to clarify the underlying reasons. While the frequency of simulation and physical experiment fit well, the simulation amplitude shows a slightly larger decrease with increasing payload when compared to the physical data.

VI. DISCUSSION

This paper introduced the minimalist monopod runner Cargo which is able to set a new benchmark in energy efficient legged locomotion on a level surface. With a TCOT of 0.0994 under experimental conditions, it outperforms the most efficient legged robot so far [5] by nearly $100\,\%$. When compared to animal walking, Cargo is able to keep up with the most efficient legged animals (African elephants with a TCOT down to 0.11 [28]). Regarding the fact that previous efficient legged robots were bipedal walkers, Cargo presents evidence that running spring mass systems can be very energy efficient too.

Parallel elastic systems allow for powerful actuation at low economic cost (most of the torque is produced by the spring and springs are much cheaper than gearboxes for the same torque) as well as safe operation, since a robot with parallel spring mechanism doesn't collapse if the power is shut down. In addition, parallel elastic actuation provides for body mass support by the springs, so the motor can be used only for energy input, which can lead to better energy efficiency. Profiting from these advantages, cargo demonstrated that the typical drawbacks of PEA, like fixed rest hip angle and the motor inertia adding up to the lower leg inertia [29], can be handled if the robot is designed adequately. Namely, due to low hopping height and low motor inertia, the impact losses remain low, and the mechanical design allows automatic adaption to different payloads and forward speeds regardless of the fixed rest length of the leg. However, a deeper investigation of the advantages of parallel elastic actuation may be beneficial, especially by clarifying if similar results could be achieved with series elastic actuation too.

In Cargo, the parallel hip spring does the large majority of the energy conversion during bouncing, while the motor only inputs positive work to overcome the various losses (see Section III-E). In addition, the spring acts as a mechanical P-controller by pulling the hip back into initial position. Together with the internal damping of hip and gearbox, this system is able to deal with large disturbances like impact or gravitational accelerations. Together with the morphology, this P-controller is able to stabilize the whole gait without any additional feedback. Therefore, Cargo is a good example how purely mechanical feedback can lead to high performance legged robots.

The fact that Cargo can handle different payloads and forward speeds without any adaptations in geometry or spring stiffness and without feedback control is quite remarkable. This ability presumes that the system is able to self-regulate its angular momentum at liftoff and therefore its landing angle at touchdown. This self regulation mechanism can be observed in simulation as well as in experiment. To clarify the properties of this mechanical feedback, further investigations are necessary.

In order to achieve superior energy efficiency, we aimed to reduce the computational power necessary by making use of a self stabilizing mechanical design and use the motor only for energy input in order to compensate for losses. The curved foot is a major contributor to Cargo's ability to self-stabilize and in fact, it even allows for static stabilization during standstill. This static stabilization is caused by the tumbler effect, with the foot radius being larger than the distance between COM and ground. As a result, no sensory feedback is necessary and all high-level computation can be done with an Arduino at very low energy consumption.

Recent work indicates that curved feet may be beneficial for running based on the spring loaded inverted pendulum (SLIP), both in terms of robustness [21], [22] and energy efficiency [21]. However, the behavior was only investigated up to a normalized foot radius of 0.7. Even though Cargo seems to profit from increased robustness and energy efficiency too, for further understanding it is necessary to close the gap in terms of normalized foot radius between actual literature (0.7) and Cargo, which has a normalized foot radius of $R_{\text{foot}}/L_{\text{leg,rest}}$ of 1.17.

At first sight, Cargo seems to travel most of the distance rolling on its large foot. However, in steady state running, part of the foot disc which is actually used does not exceed $0.078\,\text{m}$ in simulation and $0.08\,\text{m}$ in physical experiments, respectively. Compared to the leg rest length $L_{\text{leg,rest}}$ of $0.36\,\text{m}$, the effective foot length is therefore surprisingly short. In addition, the curved foot contributes only marginally to the distance traveled (see Section III-F). The contributions of the curved foot lie rather in increased robustness and probably increased energy efficiency due to reduced impact [21].

VII. CONCLUSION

This paper investigated a novel one legged payload carrier that takes advantage of parallel elastic actuation. The system is clock torque controlled, all stabilization is done mechanically. We successfully demonstrated payload transport between 0 and $150\,\text{kg}$ and a minimum TCOT below 0.1 under experimental conditions. The mechanics need no adaptation to different payloads, since any corrections can be done by varying torque amplitude and frequency of the hip motor.

At the same body weight and forward speed, Cargo features a way better TCOT than a walking human and outperforms the most efficient legged robot so far [5] by nearly $100\,\%$. Therefore, we think that it has the potential to further explore the general minimum TCOT for legged machines. In addition, it is one of the simplest machines that is able to swing its leg forward, and therefore can run freely without external support.

REFERENCES

[1] G. Gabrielli and T. Karman. What price speed? *Mechanical Engineering*, 72(10):775–781, 1950.

[2] V.A. Tucker. The energetic cost of moving about. *American Scientist*, 63:413–419, 1975.

[3] A.D. Kuo. Choosing your steps carefully. *IEEE Robotics and Automation Magazine*, 14(2):18–29, 2007.

[4] S.H. Collins and A. Ruina. A bipedal walking robot with efficient and human-like gait. In *Proc. IEEE Int. Conf. Robotics and Automation, Barcelona, Spain*, pages 1983–1988, 2005.

[5] P.A. Bhounsule, J. Cortell, and A. Ruina. Design and control of ranger: An energy efficient, dynamic walking robot. In *Proc. 15th Int. Conf. Climbing and Walking Robots (CLAWAR 2012), Baltimore, MD*, pages 441–448, 2012.

[6] D. Owaki, M. Koyama, S. Yamaguchi, S. Kubo, and A. Ishiguro. A 2-d passive-dynamic-running biped with elastic elements. *IEEE Transactions on Robotics*, 27(1):156–162, 2011.

[7] R Blickhan. The spring-mass model for running and hopping. *Journal of Biomechanics*, 22(11/12):1217–1227, 1989.

[8] T.A. McMahon and G.C. Cheng. The mechanics of running: How does stiffness couple with speed? *Journal of Biomechanics*, 23(1):65–78, 1990.

[9] G.A. Pratt and M.M. Williamson. Series elastic actuators. In *Proc. IEEE/RSJ Int. Conf. Intelligent Robotics and Systems (IROS), Pittsburgh, PA*, pages 399–406, 1995.

[10] M. Ahmadi and M. Buehler. Controlled passive dynamic running experiments with the arl-monopod ii. *IEEE Transactions on Robotics*, 22(5):974–986, 2006.

[11] D Renjewski, A. Sprowitz, A. Peekema, M. Jones, and J. Hurst. Exciting engineered passive dynamics in a bipedal robot. *IEEE Transactions on Robotics*, 31(5):1244–1251, 2015.

[12] S. Seok, A. Wang, M.Y. Chuah, D. Otten, J. Lang, and S. Kim. Design principles for highly efficient quadrupeds and implementation on the mit cheetah robot. In *Proc. IEEE Int. Conf. Robotics and Automation (ICRA), Karlsruhe, Germany*, pages 3307–3312, 2013.

[13] G. A. Folkertsma, S. Kim, and S. Stramigioli. Parallel stiffness in a bounding quadruped with flexible spine. In *Proc. IEEE/RSJ Int. Conf. Intelligent Robots and Systems (IROS), Vilamoura, Algarve, Portugal*, pages 2210–2215, 2012.

[14] M. Khoramshahi, A. Parsa, A. Ijspeert, and M.N. Ahmadabadi. Natural dynamics modification for energy efficiency: A data-driven parallel compliance design method. In *Proc. 2014 IEEE Int. Conf. Robotics and Automation (ICRA), Hong Kong, China*, pages 2412–2417, 2014.

[15] B. Brown and G. Zeglin. The bow leg hopping robot. In *Proc. IEEE Int. Conf. Robotics & Automation, Leuven, Belgium*, pages 781–786, 1998.

[16] I. Wanders, G. A. Folkertsma, and S. Stramigioli. Design and analysis of an optimal hopper for use in resonance-based locomotion. In *Proc. 2015 IEEE Int. Conf. Robotics and Automation (ICRA), Seattle, WA*, pages 5197–5202, 2015.

[17] F. Guenther, Y. Su, and F. Iida. Parallel elastic actuation for efficient large payload locomotion. In *Proc. 2015 IEEE Int. Conf. Robotics and Automation (ICRA), Seattle, WA*, pages 823–828, 2015.

[18] F. Guenther, F. Giardina, and F. Iida. Self-stable one-legged hopping using a curved foot. In *Proc. 2014 IEEE Int. Conf. Robotics and Automation (ICRA), Hong Kong, China*, pages 5133–5138, 2014.

[19] T McGeer. Passive dynamic walking. *The International Journal of Robotics Research*, 9(2):62–82, 1990.

[20] R. Ringrose. Self-stabilizing running. In *Proc. 1997 IEEE Int. Conf. Robotics and Automation, Albuquerque, New Mexico*, pages 487–493, 1997.

[21] J.Y. Jun and E. Clark. Effect of rolling on running performance. In *Proc. 2011 IEEE Int. Conf. Robotics and Automation (ICRA), Shanghai, China*, pages 2230–2235, 2011.

[22] K.J. Huang, C.K. Huang, and P.C. Lin. A simple running model with rolling contact and its role as a template for dynamic locomotion on a hexapod robot. *Bioinspir. Biomim.*, 9(4):1–20, 2014.

[23] A.H. Hansen, D.S. Childress, and E.H. Knox. Roll-over shapes of human locomotor systems: effects of walking speed. *Clinical Biomechanics*, 19:407–414, 2004.

[24] P.G. Adamczyk, S.H. Collins, and A.D. Kuo. The advantages of a rolling foot in human walking. *The Journal of Experimental Biology*, 209:3953–3963, 2006.

[25] C. Glocker and C. Studer. Formulation and preparation for numerical evaluation of linear complementarity systems. *Multibody System Dynamics*, 13(4):447–463, 2005.

[26] J. Seipel and P. Holmes. A simple model for clock-actuated legged locomotion. *Regular and Chaotic Dynamics*, 12(5):502–520, 2007.
[27] T.F. Novacheck. The biomechanics of running. *Gait and Posture*, 7:77–95, 1998.
[28] V.A. Langman, M.F. Rowe, T.J. Roberts, N.V. Langman, and C.R. Taylor. Minimum cost of transport in asian elephants: do we really need a bigger elephant? *The Journal of Experimental Biology*, 215:1509–1514, 2012.
[29] Y. Yesilevskiy, W. Xi, and C.D. Remy. A comparison of series and parallel elasticity in a monoped hopper. In *Proc. 2015 IEEE Int. Conf. Robotics and Automation (ICRA), Seattle, WA*, pages 1036–1041, 2015.

Fabian Guenther received the B.Sc. and M.Sc. degrees in mechanical engineering from the Swiss Federal Institute of Technology Zurich, Zurich, Switzerland, in 2013, where he is currently working toward the Ph.D. degree in the Bio-Inspired Robotics Laboratory. His research interests include product design, dimensioning, and actuator design for legged and fin locomotion.

Fumiya Iida received the B.S. and M.S. degrees in mechanical engineering from Tokyo University of Science, Japan in 1999, and the Dr.sc.nat. degree in informatics from the University of Zurich, Switzerland in 2006. He was a research associate with the Locomotion Laboratory, University of Jena, Germany, and with the Computer Science and Artificial Intelligence Laboratory, Massachusetts Institute of Technology, Cambridge, MA, USA. In 2009 he was appointed as an assistant professor at ETH Zurich, and from 2014 he became a lecturer at University of Cambridge, UK. He was involved in a number of research projects related to dynamic legged locomotion, navigation of autonomous robots, and humanmachine interactions. His research interests include biologically inspired robotics, embodied artificial intelligence, and biomechanics.